

pubs.acs.org/acscatalysis Research Article

# Catalytic Methane Pyrolysis with Liquid and Vapor Phase Tellurium

Jiren Zeng, Maryam Tarazkar, Tyler Pennebaker, Michael J. Gordon, Horia Metiu,\* and Eric W. McFarland\*



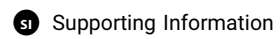
Cite This: ACS Catal. 2020, 10, 8223-8230



**ACCESS** 

Metrics & More





ABSTRACT: Methane pyrolysis transforms CH<sub>4</sub> into hydrogen and solid carbon without a CO<sub>2</sub> byproduct. Using a high-temperature liquid catalyst in a bubble column reactor, deactivation from coking is avoided and the solid carbon removed. As an element with high electron affinity, liquid tellurium is an active methane pyrolysis catalyst with an apparent activation energy of 166 kJ/mol. At the reaction temperature of approximately 1000 °C, Te has a high vapor pressure and the vapor is also found to be a catalyst with an apparent activation energy of 178 kJ/mol. Contrary to results obtained for other molten alloy catalysts, dissolving Ni in molten tellurium lowers the pyrolysis



activity. Quantum mechanical calculations were performed with accurate methods for the gas-phase reaction, and with ab initio, constant-temperature, molecular dynamics (MD) simulations with energies computed using density functional theory for the liquid phase.

KEYWORDS: heterogeneous catalysis, methane pyrolysis, tellurium, molten alloy, gas phase, carbon dioxide

#### 1. INTRODUCTION

Hydrogen is an important commodity chemical, used for ammonia and methanol production, for oil refining and for many hydrogenation reactions. It has long been imagined that clean-burning hydrogen might become an important fuel in the future. Unfortunately, most hydrogen is manufactured by the reforming of natural gas with steam, a process that produces approximately 50 million tons of hydrogen per year and generates 300 million tons of  $CO_2$  as an unavoidable byproduct.

It is possible to produce hydrogen without  $CO_2$  using methane pyrolysis,  $CH_4 \rightleftharpoons C + 2H_2$ . Some of the hydrogen produced by the pyrolysis reaction can be used to provide heat to the process, thus potentially avoiding all  $CO_2$  cogeneration. The solid carbon coproduct is readily and safely stored far easier and cheaper than capturing and storing gaseous  $CO_2$ .

Gas-phase pyrolysis of natural gas is currently used only to produce high-quality carbon black; the low-pressure hydrogen generated is used as fuel. A gas-phase process for hydrogen production by methane pyrolysis is not economically feasible because the reaction is slow at commercially accessible temperatures<sup>1–5</sup> and practical aspects of carbon removal are challenging. Much work has been devoted to the search for conventional solid, heterogeneous catalysts for pyrolysis.<sup>6–8</sup> Unfortunately, the carbon produced by the reaction poisons the catalyst, which is regenerated by burning the carbon, which produces CO<sub>2</sub>.

A strategy for avoiding the detrimental effects of carbon production uses a liquid media in a bubble column reactor. The pyrolysis reaction takes place inside the bubbles rising through the liquid column. The carbon is formed in the bubbles and can be transported to the surface of the liquid by flotation. If the liquid serves as a catalyst, when

introduced into the reactor, each bubble is in contact with a clean liquid catalyst, and the coking of the catalyst is no longer a problem. Liquid catalysts are not poisoned by impurities and do not coarsen.

Because the pyrolysis reaction is carried out at a high temperature, the molten catalysts used so far have been pure metals, metal alloys, molten salts, or mixtures of molten salts. The following molten metals have been suggested or studied experimentally: Al or an AlNi alloy, Sn, 5,11–13 Pb, 11 and Mg. Upham et al. 15 showed that high methane conversion with high hydrogen selectivity is possible using a variety of molten metal alloy catalysts in a bubble column reactor. Kang et al. 16 showed that a molten mixture of MnCl<sub>2</sub> with KCl is also an excellent catalyst and that alkali halide salts have poor performance.

Despite considerable research on methane activation, the scope of catalysts studied has been limited to several elements and compounds already known to be active, and the development of new catalysts is still largely based on trial and error, due to the lack of a clear correlation between the intrinsic properties of catalysts and their methane-activation activity. However, there have been reports of a positive correlation between the electron affinity (or equivalent) of catalysts and their catalytic activity for methane. 15,17-20 Tellurium is a metalloid with the highest electron affinity

Received: February 17, 2020 Revised: June 17, 2020 Published: July 13, 2020





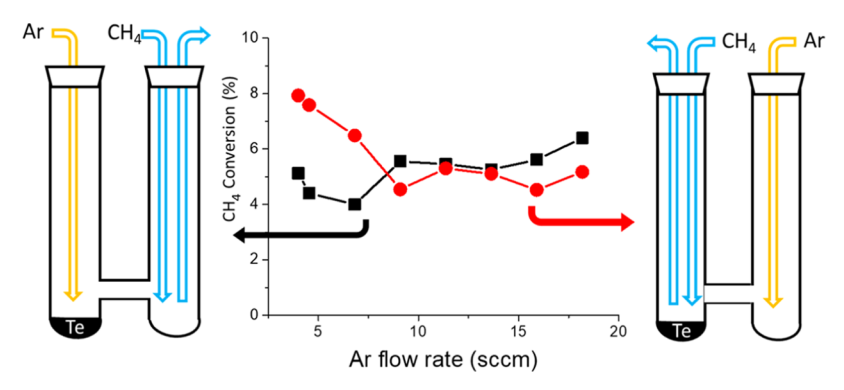


**Figure 1.** Left: the reactor used to study the reactivity of Te vapor. Right: the reactor used to study the reactivity of Te liquid and vapor. Middle: the conversion in each reactor as a function of the Ar flow rate. The reaction temperature was 1173 K. The CH<sub>4</sub> flow rate was 36 sccm, and the Ar flow rate was varied from 2 to 18 sccm (residence time in the 17 cm<sup>3</sup> reactor varied from 6.2 to 4.4 s). In control experiments without Te, no CH<sub>4</sub> conversion was detected at 1173 K under the same gas flow rate.

and electronegativity<sup>22</sup> among the common low-melting-point elemental solids and therefore might be active. Tellurium has been shown to be a dehydrogenation catalyst for several polynuclear hydrocarbons,  $^{23-25}$  but to our knowledge, it has not been studied as a catalyst for C–H bond activation in methane or CH<sub>4</sub> pyrolysis.

In this work, we present experimental and computational results regarding the catalytic activity of Te for CH4 pyrolysis, in the temperature range of 1000-1273 K. We have found the following unexpected features. (1) Te is an active liquid catalyst for methane pyrolysis. This is rather surprising because we could find no prior example in which Te catalyzes a light alkane reaction. (2) Te vapor is a pyrolysis catalyst. We are not aware of any other gas-phase catalyst for methane activation. (3) Previous work on molten metal alloys was based on the idea of using an easy-to-melt metal (e.g., Ga, In, Pb, Sn, Bi) as a solvent for a catalytically active metal (e.g., Ni, Pt, Cu). In all cases studied so far, the addition of the active metal substantially increased the activity of the "solvent"; for example, Bi is a poor pyrolysis catalyst while Ni/Bi<sup>15</sup> and Cu/Bi<sup>20</sup> alloys are among the best catalysts found so far. Surprisingly, the addition of Ni to Te significantly decreased the catalytic activity of the melt.

# 2. EXPERIMENTAL RESULTS

**2.1. Materials.** Tellurium powder (99.8% trace metal basis) was purchased from Fisher Scientific. Nickel powder (99.99% trace metal basis), bismuth shot (99.9% trace metal basis), and sodium chloride (>99%, Redi-Dri, anhydrous, ACS reagent) were purchased from Sigma-Aldrich. Gases (methane, argon, hydrogen) with ultrahigh purity (99.99%) were purchased from Airgas.

**2.2. Catalysis by the Vapor.** At a reaction temperature of 1223 K, Te has a vapor pressure of 532 Torr and a methane bubble ascending through the liquid tellurium column contains Te vapor. In addition, there is tellurium vapor in the headspace of the bubble column. It is therefore necessary to determine whether the Te vapor is a gas-phase, homogeneous catalyst for methane pyrolysis.

To determine whether Te vapor is catalytically active, the two-vessel reactor shown in Figure 1 was used to perform two kinds of experiments. In one experiment Ar was passed into the reactor arm in which Te liquid was located and methane was introduced into the other arm (see the picture at the left in Figure 1). There was only one exit port for gas (right reactor

arm in this case). The Ar entrained Te vapor into the right arm where methane was introduced. Under these conditions, methane reacted only with Te vapor. In separate experiments, Ar was introduced through the right arm of the reactor and the methane was introduced in the left arm, where the gas exit port and molten Te were located. In that experiment, methane reacts with both Te liquid and Te vapor.

The plot in the middle of Figure 1 shows methane conversion as a function of flow rate. Methane conversion was similar in both reactor configurations, and there was no detectable conversion in the control experiment in which no Te was loaded. The experiment shows that both the Te vapor and the liquid are methane pyrolysis catalysts.

Another argument that supports that at least a fraction of the methane reactions is taking place in the gas phase is that the reaction rate is the collision rate times the probability that the collision results in a reaction. From the known bubble surface area, the collision rate with the surface of the bubbles was calculated (see below). If only surface reactions were occurring, this would require the reaction probability to be greater than one. This indicates that the measured rate contains a term that is not due to the collisions with the surface; therefore, the reaction must take place in the gas phase inside the bubble.

2.3. Kinetic Measurements in a Bubble Column Reactor. The activity of several melts was measured by bubbling methane in a quartz tubular reactor containing molten liquid. In a typical experiment, 7 sccm CH<sub>4</sub> and 3 sccm Ar were premixed and bubbled through a 7 cm column of molten liquid, at various temperatures, in a quartz tube reactor with a 1.2 cm inner diameter. The initial diameter of the bubbles was approximately 5 mm. From measuring the rise velocity, we calculated a bubble residence times in the liquid of approximately 0.5 s. The composition of the effluent gas was analyzed with an SRS RGA 200 mass spectrometer. The temperature was varied between 1173 and 1253 K. The temperature dependence of methane conversion under these conditions is shown in Figure 2 for molten NaCl, Te,  $\text{Ni}_{0.5}\text{Te}_{0.5}\text{,}$  and  $\text{Ni}_{0.27}\text{Te}_{0.73}\text{.}$  For comparison, we also show the performance of molten Ni<sub>0.27</sub>Bi<sub>0.73</sub>, which is the most active molten metal found prior to this work. 15 All telluriumcontaining melts studied so far are more active than Ni<sub>0.27</sub>Bi<sub>0.73</sub>.

Prior work<sup>15</sup> has shown that easy-to-melt metals, such as In, Bi, Sn, Ga, and Pb, are poor catalysts. Dissolving Cu, Ni, or Pt in molten In, Bi, Sn, Ga, or Pb increased substantially the

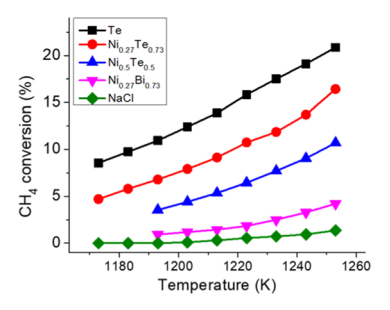


**Figure 2.** CH<sub>4</sub> conversions in 7 cm bubble column reactors. The partial pressure of CH<sub>4</sub> was 0.7 atm, the bubble diameter was  $\sim$ 5 mm, and the residence time was approximately 0.5 s.

catalytic activity and led to the suggestion that In, Bi, Sn, Ga, and Pb are, more or less, inert solvents and Cu, Ni, and Pt are active components. We expected that a similar increase might be obtained by dissolving Ni in Te. Surprisingly, we found that tellurium activity decreases upon the addition of Ni to the melt (see Figure 2). The specific origin of the decreased activity may arise from a lower surface concentration of Te accessible to the gas-phase methane, specific electronic interactions between Te and Ni, and/or the decreased concentrations of gas-phase Te present in the bubble.

**2.4. Kinetic Modeling.** After being filled with a mixture of methane and Ar carrier gas, the bubble travels upwards through the molten Te column. It is difficult to build a detailed kinetic model for pyrolysis in the high-temperature bubble column because several processes occur concomitantly. (1) Tellurium evaporates and produces Te vapor inside the bubble. (2) As the pyrolysis reaction proceeds, there is the time-dependent formation of solid carbon, which adheres to the wall of the bubble blocking some of the bubble surface areas. From the carbon balance, we know that sufficient carbon is formed to produce multilayers. (3) The process is further complicated by the fact that carbon is a pyrolysis catalyst. The catalytic activity of carbon is substantially lower than that of tellurium, but it would be incorrect to think of carbon as a mere surface blocker. (4) As the reaction proceeds and the total number of moles of gas increases (2 mol of H2 are produced per mole of CH<sub>4</sub> consumed), the volume of the bubble increases. (5) There is likely some (unknown) solubility of hydrogen in the liquid tellurium, and there is no information regarding the rate of this process.

Despite the complexities of the reacting system, useful information for comparisons of different catalysts can be obtained from apparent activation energies and effective first-order rate constants obtained in a differential reactor configuration. An assumption that the reaction kinetics can be defined by a first-order rate constant is consistent with the widely accepted assumption that breaking the C—H bond is the rate-limiting step. In the present context, the measurements tell us that regardless of the mechanism, the bubble column is more efficient than the vapor alone and that in a bubble most of the catalytic activity is due to the liquid surface.

For a differential bubble column reactor operating at very low methane conversion X, the apparent rate constant k is

$$k_{\rm apparent} = \frac{{\rm reaction \, rate}}{{\rm [CH_4]}} \approx \frac{{\rm d}X}{{\rm d}t} \approx \frac{{\rm conversion}}{{\rm residence \, time}}$$
 (1)

where the reaction rate is measured in mol/m³/s and the methane concentration, [CH<sub>4</sub>], changes minimally over the

residence time,  $\tau$ , which is the rise time of the bubble in the reactor. For the reaction in the vapor phase in the differential two-vessel reactor, the apparent second-order rate constant in the differential reactor is

$$k_{\rm apparent} = \frac{{\rm reaction \, rate}}{{\rm [CH_4][Te]}} = \frac{{\rm conversion}}{{\rm residence \, time} \, \times \, {\rm [Te]}}$$

where the tellurium concentration is proportional to the partial pressure of the tellurium vapor. In general, the reaction rate of a catalytic process is proportional to the number of active sites; here, the number of active sites is proportional to the partial pressure of Te and the vapor pressure is temperature-dependent.<sup>26</sup>

In Figure 3, we plot the log of conversion/residence time versus  $10^4/RT$  for both bubble column and two-vessel reactor,

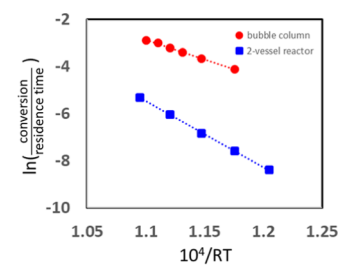


**Figure 3.** Plot of  $\ln \frac{\text{conversion}}{\text{residence time}}$  versus  $\frac{10^4}{RT}$  for the reaction with the Te vapor catalyst (blue squares) and in the bubble column containing molten Te (red circles). Data were obtained in a differential reactor with a residence time of approximately 5 s for a two-vessel reactor and 0.5 s for a bubble column. R is the ideal gas constant and T is the temperature.

where R is the ideal gas constant and T is the temperature. For bubble columns, this is the same as an Arrhenius plot if we assume that the major catalyst is liquid Te and the contribution from Te vapor is negligible. For the two-vessel reactor, where the major contribution comes from Te vapor, it is not an Arrhenius plot because the amount of catalyst (Te vapor) is temperature-dependent. This plot shows that the reaction rate is higher in a bubble column than when using a Te-vapor catalyst in a two-vessel reactor. The apparent activation energies and the Arrhenius pre-exponential factors in the effective rate constants are shown in Table 1, which shows that the Te vapor catalyst is more active than pure gasphase  $CH_4$  pyrolysis without a catalyst.

**2.5. Catalyst Stability.** Using molten and gaseous Te as catalysts avoids two of the main disadvantages of solid catalysts for pyrolysis: there is no loss of activity due to coking or to coarsening. However, some deterioration is possible if feed

Table 1. Kinetic Data of  $CH_4$  Pyrolysis in Different Systems Measured Between 973 and 1253 K

composition	apparent $E_a$ (kJ/mol)	pre-exponential factor	
Te bubble column	166	$4.9 \times 10^6 \text{ s}^{-1}$	
$Ni_{0.27}Te_{0.73}$	193	$1.8 \times 10^7 \text{ s}^{-1}$	
$Ni_{0.5}Te_{0.5}$	223	$4.7 \times 10^8 \text{ s}^{-1}$	
$Ni_{0.27}Bi_{0.73}$	208	$6.5 \times 10^5 \text{ s}^{-1}$	
NaCl	374	$3.9 \times 10^{12} \text{ s}^{-1}$	
no catalyst <sup>27</sup>	423	$5.1 \times 10^{14} \text{ s}^{-1}$	
Te vapor	178	$4.4 \times 10^6 \text{ m}^3/\text{mol/s}$	

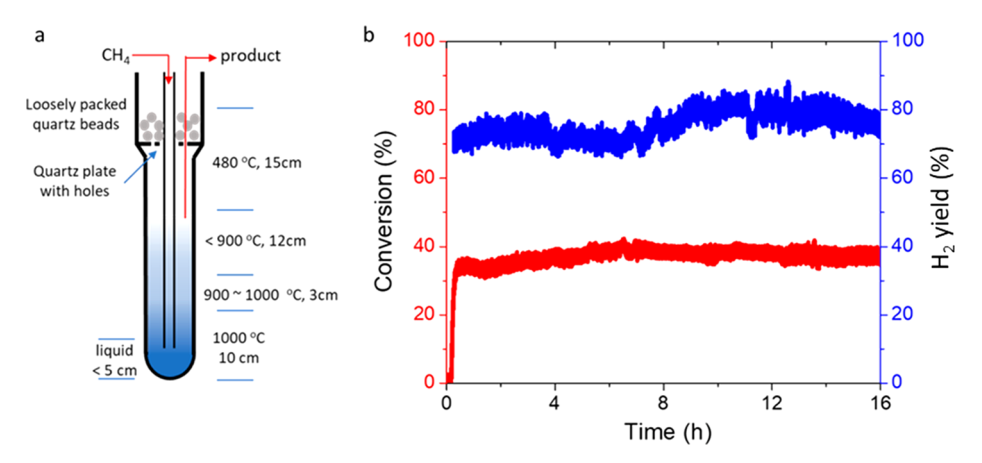


Figure 4. (a) Schematic representation of the reflux reactor. (b) Methane conversion (red) and  $H_2$  yield (blue) of pyrolysis in the reflux reactor. Residence time in the hot zone (900–1000 °C) is less than 12 s.

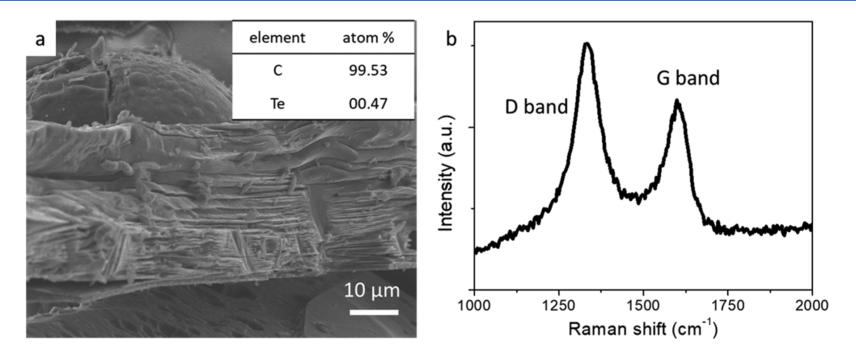


Figure 5. (a) SEM image of the carbon collected from the reflux reactor after heat treatment. The inset shows the EDS element analysis for this carbon sample. (b) Raman spectrum of the carbon collected from the reflux reactor.

impurities build up or if any carbon residues dissolve/disperse in the liquid and modify its composition and mechanical properties. We investigated the stability of the Te catalyst over a 16 h period. To prevent loss of catalyst in the vapor phase, we used a reflux configuration (Figure 4a) containing 15 g of Te ( $\sim$ 5 cm column height). The reactant gas (7 sccm CH<sub>4</sub>) and an inert gas (3 sccm argon) were introduced at the bottom of the reactor, which was maintained at 1273 K, slightly above the boiling point of Te (1263 K). The temperature of the middle part of the reactor was less than 1173 K, and the temperature at the top part of the reactor was 753 K, slightly higher than the melting point of Te (which is 723 K). The volume of the reactor in the hot zone (1173-1273 K) was 15 cm<sup>3</sup>. Methane conversion and hydrogen yield were stable for 16 h (Figure 4b). During this time, the conversion was 37%, with a hydrogen yield of 70-80% (Figure 4b). Since the reactor was run at steady state and both vaporization and condensation of Te took place in the reactor, we do not know the partial pressure of Te in the gas, but it should be reasonably high due to its high vapor pressure. Based on gas flow rate, reactor volume, and temperature, the calculated maximum residence time of CH<sub>4</sub> is 12 s assuming low Te vapor pressure, but the actual residence time should be shorter.

Although no  $C_2$ – $C_5$  compounds were detected during the stability test, small amounts of relatively stable aromatics and polycyclic aromatics, including benzene, toluene, naphthalene, anthracene, pyrene, and other compounds, were detected. This suggests that after the C–H bond in methane is broken, polycyclic aromatic hydrocarbons are formed. Because of this, the hydrogen yield is less than 100%. It is known<sup>28–30</sup> that the

rate of dehydrogenation of polyaromatics is higher than that of methane dehydrogenation. Therefore, we attribute their presence in the effluent to the very short residence time and low conversion.

2.6. Solid Carbon Characterization. The solid carbon generated by pyrolysis contains Te. The contamination level of Te in carbon was dependent on where the carbon was collected. The carbon collected in the 900–1000  $^{\circ}\text{C}$  zone contained more than 2 atom % Te, whereas the carbon collected in low-temperature zones where condensation of Te took place contained even more Te. To remove Te, we baked all collected carbon in a tube furnace at 1273 K for 10 h, in Ar. This reduces the amount of Te in the carbon to less than 0.5 atom %. Scanning electron microscopy (SEM) (Thermo Fisher Apreo C LoVac) and energy-dispersive X-ray spectroscopy (EDS) were used to characterize the morphology and purity of the carbon. Raman spectroscopy (Horiba Jobin Yvon LabRAM Aramis) was performed using a 633 nm laser wavelength, to characterize the extent of graphitization of the carbon. Electron microscopy shows (Figure 5a) that the carbon has a layered structure on the scale of 10  $\mu$ m, consistent with sp<sup>2</sup> carbon. The Raman spectrum (Figure 5b) of the carbon samples contains a clear D band and a G band, which are signatures of sp<sup>2</sup> graphitic carbon. The broadening of the D peak and the high-intensity ratio of D-G indicate that the carbon is disordered.3

## 3. COMPUTATIONAL RESULTS

**3.1. Electronic Structure Calculations.** We performed electronic structure calculations for the reaction of methane

with gaseous and liquid tellurium. Te vapor consists mostly of Te dimers. For examining some aspects of the reaction of a Te<sub>2</sub> cluster with methane, we used the coupled-cluster single double (CCSD) method.<sup>32</sup> The structure of the molecules involved was optimized using the second-order Møller–Plesset perturbation theory (MP2).<sup>33</sup> The correlation consistent-polarized valence double zeta (cc-pvdz) basis set<sup>34</sup> that we used for carbon is composed of 14 functions, (9s4p1d)/[3s2p1d]. Five functions (4s1p)/[2s1p] were used for the hydrogen. For Te atoms, we used a correlation consistent-polarized valence quadruple zeta basis set with a relativistic pseudopotential (cc-pvqz-pp)<sup>35</sup> composed of (14s11p12d2f1g) Gaussian type functions, contracted to [6s6p4d2f1g]. The calculations of Te<sub>2</sub> properties were performed with the Gaussian computational package,<sup>36</sup> and the visualization was performed with MacMolPlt.<sup>37</sup>

Ab initio, constant-temperature, molecular dynamics (MD) simulations 38-40 for liquid Te were performed with the VASP program. 41-44 The energy for the molecular dynamics simulations was provided by density functional theory (DFT), using a plane-wave basis set with a 350 eV energy cutoff, a  $(2 \times 2 \times 1)$  Monkhorst-Pack k-point grid to sample reciprocal space, the PBE functional, 45 and D3 van der Waals correction.46 In our simulations, we model a molten Te (composed of 70 atoms) in the slab. Thus, liquid Te has one vacuum-Te interface. The motion of the atoms is treated classically, and the time steps of 1 fs are used to solve the Nosé equations of motion. The Nosé thermostat was set to keep the temperature around 1300 K. We used the projector augmented-wave method 47,48 and included six valence electrons for Te atoms, four electrons for carbon, and one electron for H; the remaining electrons in the atoms were treated with the frozen core approximation. Spin-paired (nonspin-polarized) DFT calculations were performed for all molecular dynamic simulations of the melt. Similar calculations have been performed for liquid Te<sup>49-52</sup> but none examined methane chemistry at the liquid surface.

The mean internal energy in constant-temperature molecular dynamics is given by

$$\langle E \rangle_{t} = \frac{1}{t - t_0} \int_{t_0}^{t} E(\tau) d\tau$$
(3)

where  $E(\tau)$  is the total internal energy at time  $\tau$ . Since the system is held at a constant temperature, the total energy fluctuates as time evolves. The simulation prior to the time  $t_0$  is used to equilibrate the system and is not included in the average energy.

**3.2. Methane Activation by Liquid Tellurium.** It is generally accepted that the rate-limiting step in methane activation is the breaking of the C–H bond and that all subsequent reaction steps have a substantially higher rate. To calculate the activation energy of methane dissociation on molten tellurium, we selected a configuration from a long molecular dynamics run (at 14 ps), and we then froze 75% of the atoms in the simulation located at the bottom of the slab and optimized the atomic positions of the remaining 25% of the atoms. In this way, we created a "glassy" solid whose structure is similar to that of the liquid. We then situated the dissociated methane species (\*H and \*CH<sub>3</sub>) in different sites on the surface and minimized the energy again. Different configurations included coordinating the absorbed fragment to different metal atoms. The binding energy for more than 10

different configurations on Te liquid was computed using the equation

$$E_{\text{ads}} = E_{({^*CH_3} + {^*H})/\text{Te}(1)} - E_{\text{Te}(1)} - E_{\text{CH}_4(g)}$$
 (4)

 $E_{(^*\mathrm{CH}_3+^*\mathrm{H})/\mathrm{Te}\,(1)}$  is the total energy of Te liquid with H and CH $_3$  adsorbed on the surface,  $E_{\mathrm{Te}\,(1)}$  is the energy of the liquid in the absence of methane, and  $E_{\mathrm{CH}_4\,(\mathrm{g})}$  is the energy of gasphase methane. Overall, the binding energy varies  $\sim\!0.6$  eV based on the position of the \*H and \*CH $_3$  species on the surface of tellurium liquid. Figure 6 shows schematically the energy of several bonding configurations for CH $_3$  and H bound to the liquid surface.

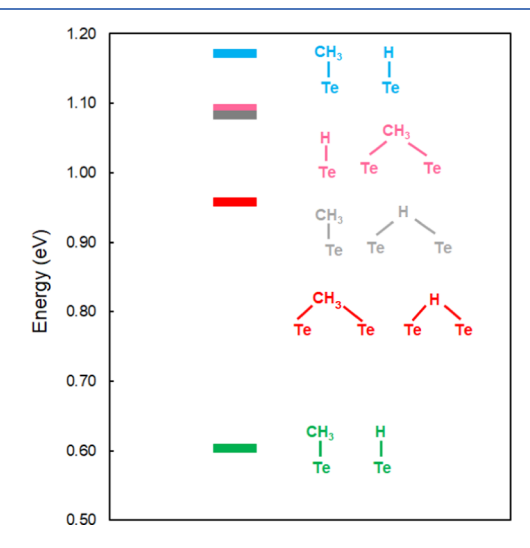


**Figure 6.** Calculated binding energy of methane on the surface of liquid tellurium for the five most stable configurations of \*H and  $^*CH_3$  adsorbed on tellurium. The structures were taken at t = 14 ps.

According to the Brønsted-Evans-Polanyi rule, 53 the reaction with the lowest activation energy is likely to be the one for which the final state has the lowest energy. In Figure 6, this is the state in which both CH3 and H are bonded to one Te atom in the surface of the liquid. In Figure 7, we show the lowest energy path for the reaction \*CH<sub>4</sub> → \*CH<sub>3</sub> + \*H, where the notation \*A indicates that the species A is adsorbed on the surface. The energy along the reaction path was calculated with the nudged elastic band method, for a process in which the system starts as methane adsorbed on the liquid and dissociates to form the lowest energy configuration shown in Figure 6. The calculated activation energy of the reaction  $*CH_4 \rightarrow *CH_3 + *H$  is 1.45 eV (139 kJ/mol). The effective activation energy measured in the bubble column is 166 kJ/ mol (see Table 1). The activation energy at the liquid surface depends on the surface site where the dissociation occurs. Since we have calculated the lowest activation energy (the one for reaching the most stable dissociated state), the calculated value should be lower than the measured one. Considering the error inherent in the density functional calculations and the variety of adsorption sites, one would not expect closer agreement.

**3.3.** Activation Energy for Methane Dissociation by Gas-Phase Tellurium. Our calculations show that the lowest energy compound formed by the reaction of Te<sub>2</sub> with methane is CH<sub>3</sub>—Te—Te—H. The energies, entropies, and free energies of several reactions of this compound are listed in Table 2. The

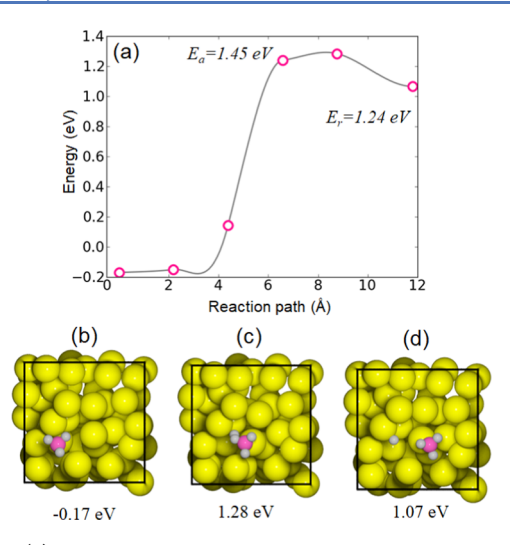


Figure 7. (a) Reaction path for methane dissociation on the surface of liquid Te. (b) Initial atomic configuration and the energy of methane adsorbed on the surface of liquid Te. (c) Transition state energy and configuration for  $CH_4$  dissociation. (d) Dissociated state consisting of adsorbed  $CH_3$  and adsorbed H.

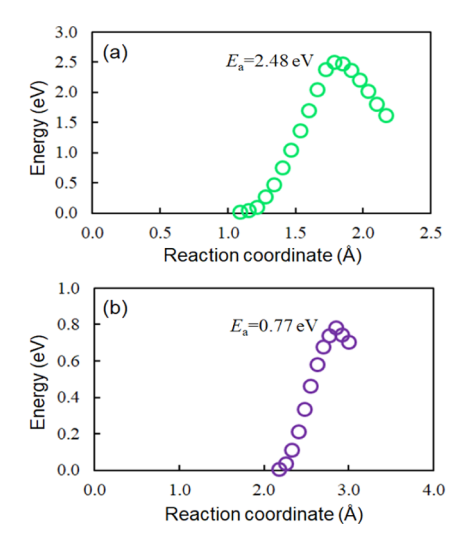
free energy favors the reaction  $CH_3$ —Te—Te— $H \to Te$ —Te— $H + • CH_3$  with  $CH_3$ —Te—Te— $H \to Te$ — $CH_3 + Te$ —H almost as probable.

The reaction path of  $CH_4 + Te_2 \rightarrow CH_3 - Te - Te - H$  is shown in Figure 8. The calculated activation energy is 2.48 eV (239 kJ/mol) while the measured effective activation energy is 178 kJ/mol. Since the method of calculation of the activation energy is fairly accurate, the discrepancy may be attributed, in part, to the fact that the effective activation energy might not be exactly the activation energy of the rupture of the C-H bond. The imaginary frequencies for the transition state are given in Table S1, and the geometry of the transition state is shown in Figure S1 in the Supporting Information.

Due to the known shortcomings of DFT, the calculated activation energies are not quantitatively reliable. However, the qualitative difference between the values of the reaction catalyzed by the liquid and that catalyzed by the vapor is significant. It shows that the vapor is an inferior catalyst.

## 4. CONCLUSIONS

As an element with high electron affinity, molten tellurium is an active methane pyrolysis catalyst with an apparent activation energy of 166 kJ/mol. Methane conversion of over 30% was obtained at residence times of less than 12 s at temperatures between 1100 and 1250 K, which is very close to the Te boiling temperature of 1261 K. Since the vapor pressure of Te at these temperatures is very high, experiments showed that the vapor itself is a catalyst but substantially less efficient than the liquid. As a liquid catalyst, Te when mixed with increasing



amounts of Ni was observed to be less active, which if the opposite of the observations made of Bi when increasing amounts of Ni or Cu are added. Given the relatively low activity of Te vapor, its high vapor pressure is a drawback for practical implementation: Te vapor escaping a bubble column reactor needs to be condensed and recovered. A possible solution is the use of a reflux reactor; however, given the fact that Te is rare, volatile, and expensive, it is unlikely that it will be used in large-scale commercial applications.

### ASSOCIATED CONTENT

## Supporting Information

The Supporting Information is available free of charge at https://pubs.acs.org/doi/10.1021/acscatal.0c00805.

Imaginary frequencies for the transition states for two reactions (Table S1) and schematic of the geometry of the transition states (Figure S1) (PDF)

## AUTHOR INFORMATION

#### **Corresponding Authors**

Horia Metiu — Department of Chemistry and Biochemistry, University of California, Santa Barbara, Santa Barbara, California 93106; ⊚ orcid.org/0000-0002-3134-4493; Email: metiu@chem.ucsb.edu

Eric W. McFarland — Department of Chemical Engineering, University of California, Santa Barbara, Santa Barbara, California 93106, United States; orcid.org/0000-0001-7242-509X; Email: mcfar@ucsb.edu

Table 2. Energy, Entropy, and Free Energy of Various Reactions Taking Place After the Reaction of Te<sub>2</sub> with CH<sub>4</sub> to Form H-Te-Te-CH<sub>3</sub>

	reaction	$\Delta H_0^{1023  \mathrm{K}}  (\mathrm{kJ/mol})$	$T\Delta S_0^{1023 \text{ K}} \text{ (kJ/mol)}$	$\Delta G_0^{1023  \mathrm{K}}  (\mathrm{kJ/mol})$
(1)	$CH_3$ -Te-Te-H $\rightarrow \bullet$ [Te-CH <sub>3</sub> ] + $\bullet$ [Te-H]	+160	+131	+29
(2)	$CH_3$ -Te-Te-H $\rightarrow \bullet$ [Te-H] + $\bullet$ CH <sub>3</sub> +Te	+348	+255	+93
(3)	$CH_3$ -Te-Te-H $\rightarrow \bullet$ [Te- $CH_3$ ] + $\bullet$ H + Te	+386	+227	+159
(4)	$CH_3$ -Te-Te-H $\rightarrow \bullet$ [Te-Te-H] + $\bullet$ CH <sub>3</sub>	+180	+159	+21
(5)	$CH_3$ -Te-Te-H $\rightarrow \bullet [Te-Te-CH_3] + \bullet H$	+212	+118	+94

#### **Authors**

- Jiren Zeng Department of Chemistry and Biochemistry, University of California, Santa Barbara, Santa Barbara, California 93106
- Maryam Tarazkar Department of Chemistry and Biochemistry, University of California, Santa Barbara, Santa Barbara, California 93106
- Tyler Pennebaker College of Creative Studies, University of California, Santa Barbara, Santa Barbara, California 93106, United States
- Michael J. Gordon Department of Chemical Engineering, University of California, Santa Barbara, Santa Barbara, California 93106, United States; orcid.org/0000-0003-0123-9649

Complete contact information is available at: https://pubs.acs.org/10.1021/acscatal.0c00805

#### **Author Contributions**

<sup>∥</sup>J.Z. and M.T. contributed equally to this work. **Notes** 

The authors declare no competing financial interest.

## ACKNOWLEDGMENTS

This work was primarily supported by the Energy & Biosciences Institute through the EBI-Shell program and the U.S. Department of Energy, Office of Science, Basic Energy Sciences, Grant no. DE-FG03-89ER14048. Use was made of computational facilities purchased with funds from the National Science Foundation (CNS-1725797) and administered by the Center for Scientific Computing (CSC). The CSC is supported by the California NanoSystems Institute and the Materials Research Science and Engineering Center (MRSEC; NSF DMR 1720256) at UC Santa Barbara. The authors are grateful for the invaluable assistance of Richard Bock who constructed the quartz reactor vessels.

## REFERENCES

- (1) Olsvik, O.; Rokstad, O. A.; Holmen, A. Pyrolysis of methane in the presence of hydrogen. *Chem. Eng. Technol.* **1995**, *18*, 349–358.
- (2) Abanades, S.; Flamant, G. High-temperature solar chemical reactors for hydrogen production from natural gas cracking. *Chem. Eng. Commun.* **2008**, *195*, 1159–1175.
- (3) Abánades, A.; Ruiz, E.; Ferruelo, E. M.; Hernández, F.; Cabanillas, A.; Martínez-Val, J. M.; Rubio, J. A.; López, C.; Gavela, R.; Barrera, G.; Rubbia, C.; Salmieri, D.; Rodilla, E.; Gutiérrez, D. Experimental analysis of direct thermal methane cracking. *Int. J. Hydrogen Energy* **2011**, *36*, 12877–12886.
- (4) Abánades, A.; Rubbia, C.; Salmieri, D. Thermal cracking of methane into hydrogen for a CO<sub>2</sub>-free utilization of natural gas. *Int. J. Hydrogen Energy* **2013**, 38, 8491–8496.
- (5) Abánades, A.; Rathnam, R. K.; Geißler, T.; Heinzel, A.; Mehravaran, K.; Müller, G.; Plevan, M.; Rubbia, C.; Salmieri, D.; Stoppel, L.; Stückrad, S.; Weisenburger, A.; Wenninger, H.; Wetzel, T. Development of methane decarbonisation based on liquid metal technology for CO<sub>2</sub>-free production of hydrogen. *Int. J. Hydrogen Energy* **2016**, *41*, 8159–8167.
- (6) Li, Y.; Li, D.; Wang, G. Methane decomposition to  $CO_x$ -free hydrogen and nano-carbon material on group 8–10 base metal catalysts: A review. *Catal. Today* **2011**, *162*, 1–48.
- (7) Holladay, J. D.; Hu, J.; King, D. L.; Wang, Y. An overview of hydrogen production technologies. *Catal. Today* **2009**, *139*, 244–260.
- (8) Choudhary, T. V.; Aksoylu, E.; Goodman, D. W. Nonoxidative activation of methane. *Catal. Rev.* **2003**, *45*, 151–203.
- (9) Oblad, A. G.; Milliken, T. G., Jr.; Boedeker, E. R. Production of Hydrogen and Carbon. U.S. Patent US2,760,847A1956.

- (10) Steinberg, M. Fossil fuel decarbonization technology for mitigating global warming. *Int. J. Hydrogen Energy* **1999**, 24, 771–777.
- (11) Serban, M.; Lewis, M. A.; Marshall, C. L.; Doctor, R. D. Hydrogen production by direct contact pyrolysis of natural gas. *Energy Fuels* **2003**, *17*, 705–713.
- (12) Plevan, M.; Geißler, T.; Abánades, A.; Mehravaran, K.; Rathnam, R. K.; Rubbia, C.; Salmieri, D.; Stoppel, L.; Stückrad, S.; Wetzel, T. Thermal cracking of methane in a liquid metal bubble column reactor: Experiments and kinetic analysis. *Int. J. Hydrogen Energy* **2015**, *40*, 8020–8033.
- (13) Geißler, T.; Plevan, M.; Abánades, A.; Heinzel, A.; Mehravaran, K.; Rathnam, R. K.; Rubbia, C.; Salmieri, D.; Stoppel, L.; Stückrad, S.; Weisenburger, A.; Wenninger, H.; Wetzel, T. Experimental investigation and thermo-chemical modeling of methane pyrolysis in a liquid metal bubble column reactor with a packed bed. *Int. J. Hydrogen Energy* **2015**, *40*, 14134–14146.
- (14) Wang, K.; Li, W. S.; Zhou, X. P. Hydrogen generation by direct decomposition of hydrocarbons over molten magnesium. *J. Mol. Catal. A: Chem.* **2008**, 283, 153–157.
- (15) Upham, D. C.; Agarwal, V.; Khechfe, A.; Snodgrass, Z. R.; Gordon, M. J.; Metiu, H.; McFarland, E. W. Catalytic molten metals for the direct conversion of methane to hydrogen and separable carbon. *Science* **2017**, *358*, 917–921.
- (16) Kang, D.; Rahimi, N.; Gordon, M. J.; Metiu, H.; McFarland, E. W. Catalytic methane pyrolysis in molten MnCl<sub>2</sub>-KCl. *Appl. Catal., B* **2019**, 254, 659–666.
- (17) Horn, R.; Schlögl, R. Methane activation by heterogeneous catalysis. *Catal. Lett.* **2015**, *145*, 23–29.
- (18) Che, F.; Gray, J. T.; Ha, S.; McEwen, J.-S. Improving Ni catalysts using electric fields: a DFT and experimental study of the methane steam reforming reaction. ACS Catal. 2017, 7, 551–562.
- (19) Che, F.; Ha, S.; McEwen, J. S. Catalytic Reaction Rates Controlled by Metal Oxidation State: C–H Bond Cleavage in Methane over Nickel-Based Catalysts. *Angew. Chem.* **2017**, *129*, 3611–3615.
- (20) Palmer, C.; Tarazkar, M.; Kristoffersen, H. H.; Gelinas, J.; Gordon, M. J.; McFarland, E. W.; Metiu, H. Methane Pyrolysis with a Molten Cu–Bi Alloy Catalyst. *ACS Catal.* **2019**, *9*, 8337–8345.
- (21) Myers, R. T. The periodicity of electron affinity. *J. Chem. Educ.* **1990**, *67*, 307–308.
- (22) Little, E. J., Jr.; Jones, M. M. A complete table of electronegativities. J. Chem. Educ. 1960, 37, 231–233.
- (23) Takahashi, K.; Ogino, Y. Liquid tellurium as a catalyst for the dehydrogenation of several polynuclear hydrocarbons. *Chem. Lett.* **1978**, *7*, 423–425.
- (24) Takahashi, K.; Ogino, Y. Studies on the catalysis of molten metal. 13. Kinetics of dehydrogenation of tetralin over molten tellurium catalyst. *Fuel* **1981**, *60*, 975–979.
- (25) Takahashi, K.; Ogino, Y. Promoting effect of selenium on the catalysis of liquid tellurium in the dehydrogenation of polynuclear hydrocarbons. *Chem. Lett.* **1978**, *7*, 549–552.
- (26) Ubelis, A. P. Temperature dependence of the saturated vapor pressure of tellurium. *J. Eng. Phys.* **1982**, *42*, 309–315.
- (27) Skinner, G. B.; Ruehrwein, R. A. Shock tube studies on the pyrolysis and oxidation of methane. *J. Phys. Chem. A* **1959**, *63*, 1736–1742.
- (28) Kinney, C. R.; DelBel, E. Pyrolytic behavior of unsubstituted aromatic hydrocarbons. *Ind. Eng. Chem.* **1954**, *46*, 548–556.
- (29) Kwon, Y.; Kim, T. Y.; Kwon, G.; Yi, J.; Lee, H. Selective activation of methane on single-atom catalyst of rhodium dispersed on zirconia for direct conversion. *J. Am. Chem. Soc.* **2017**, *139*, 17694–17699.
- (30) Marsh, H.; Martínez-Escandell, M.; Rodríguez-Reinoso, F. Semicokes from pitch pyrolysis: mechanisms and kinetics. *Carbon* **1999**, 37, 363–390.
- (31) Sadezky, A.; Muckenhuber, H.; Grothe, H.; Niessner, R.; Pöschl, U. Raman microspectroscopy of soot and related carbonaceous materials: Spectral analysis and structural information. *Carbon* **2005**, *43*, 1731–1742.

ACS Catalysis pubs.acs.org/acscatalysis Research Article

- (32) Purvis, G. D., III; Bartlett, R. J. A full coupled-cluster singles and doubles model: The inclusion of disconnected triples. *J. Chem. Phys.* **1982**, *76*, 1910–1918.
- (33) Head-Gordon, M.; Pople, J. A.; Frisch, M. J. MP2 energy evaluation by direct methods. *Chem. Phys. Lett.* **1988**, *153*, 503–506. (34) Dunning, T. H., Jr. Gaussian basis sets for use in correlated molecular calculations. I. The atoms boron through neon and hydrogen. *J. Chem. Phys.* **1989**, *90*, 1007–1023.
- (35) Peterson, K. A.; Figgen, D.; Goll, E.; Stoll, H.; Dolg, M. Systematically convergent basis sets with relativistic pseudopotentials. II. Small-core pseudopotentials and correlation consistent basis sets for the post-d group 16–18 elements. *J. Chem. Phys.* **2003**, *119*, 11113–11123.
- (36) Frisch, M. J.; Trucks, G. W.; Schlegel, H. B.; Scuseria, G. E.; Robb, M. A.; Cheeseman, J. R.; Scalmani, G.; Barone, V.; Petersson, G. A.; Nakatsuji, H.; Li, X.; Caricato, M.; Marenich, A. V.; Bloino, J.; Janesko, B. G.; Gomperts, R.; Mennucci, B.; Hratchian, H. P.; Ortiz, J. V.; Izmaylov, A. F.; Sonnenberg, J. L.; Williams; Ding, F.; Lipparini, F.; Egidi, F.; Goings, J.; Peng, B.; Petrone, A.; Henderson, T.; Ranasinghe, D.; Zakrzewski, V. G.; Gao, J.; Rega, N.; Zheng, G.; Liang, W.; Hada, M.; Ehara, M.; Toyota, K.; Fukuda, R.; Hasegawa, J.; Ishida, M.; Nakajima, T.; Honda, Y.; Kitao, O.; Nakai, H.; Vreven, T.; Throssell, K.; Montgomery, J. A., Jr.; Peralta, J. E.; Ogliaro, F.; Bearpark, M. J.; Heyd, J. J.; Brothers, E. N.; Kudin, K. N.; Staroverov, V. N.; Keith, T. A.; Kobayashi, R.; Normand, J.; Raghavachari, K.; Rendell, A. P.; Burant, J. C.; Iyengar, S. S.; Tomasi, J.; Cossi, M.; Millam, J. M.; Klene, M.; Adamo, C.; Cammi, R.; Ochterski, J. W.; Martin, R. L.; Morokuma, K.; Farkas, O.; Foresman, J. B.; Fox, D. J. Gaussian 16, rev. B.01; Gaussian Inc.: Wallingford, CT, 2016.
- (37) Bode, B. M.; Gordon, M. S. MacMolPlt: a graphical user interface for GAMESS. *J. Mol. Graphics Modell.* **1998**, *16*, 133–138. (38) Nosé, S. A molecular dynamics method for simulations in the canonical ensemble. *Mol. Phys.* **2002**, *100*, 191–198.
- (39) Nosé, S. A molecular dynamics method for simulations in the canonical ensemble. *Mol. Phys.* **1984**, *52*, 255–268.
- (40) Nosé, S. A unified formulation of the constant temperature molecular dynamics methods. *J. Chem. Phys.* **1984**, *81*, 511–519.
- (41) Kresse, G. Ab initio molecular dynamics for liquid metals. J. Non-Cryst. Solids 1995, 192–193, 222–229.
- (42) Kresse, G.; Furthmüller, J. Efficiency of ab-initio total energy calculations for metals and semiconductors using a plane-wave basis set. *Comput. Mater. Sci.* **1996**, *6*, 15–50.
- (43) Kresse, G.; Furthmüller, J. Efficient iterative schemes for ab initio total-energy calculations using a plane-wave basis set. *Phys. Rev.* B 1996, 54, No. 11169.
- (44) Kresse, G.; Hafner, J. Ab initio molecular-dynamics simulation of the liquid-metal-amorphous-semiconductor transition in germanium. *Phys. Rev. B* **1994**, *49*, No. 14251.
- (45) Perdew, J. P.; Burke, K.; Ernzerhof, M. Generalized gradient approximation made simple. *Phys. Rev. Lett.* **1996**, *77*, No. 3865.
- (46) Grimme, S.; Antony, J.; Ehrlich, S.; Krieg, H. A consistent and accurate ab initio parametrization of density functional dispersion correction (DFT-D) for the 94 elements H-Pu. *J. Chem. Phys.* **2010**, 132, No. 154104.
- (47) Blöchl, P. E. Projector augmented-wave method. *Phys. Rev. B* **1994**, *50*, No. 17953.
- (48) Kresse, G. J.; Joubert, D. From ultrasoft pseudopotentials to the projector augmented-wave method. *Phys. Rev. B* **1999**, *59*, No. 1758.
- (49) Stadler, R.; Gillan, M. J. First-principles molecular dynamics studies of liquid tellurium. *J. Phys.: Condens. Matter* **2000**, *12*, 6053–6061.
- (50) Akola, J.; Jones, R. O.; Kohara, S.; Usuki, T.; Bychkov, E. Density variations in liquid tellurium: Roles of rings, chains, and cavities. *Phys. Rev. B* **2010**, *81*, No. 094202.
- (51) Zhao, G.; Liu, C. S.; Zhu, Z. G. Ab initio molecular dynamics simulations on structure change of liquid Te from normal- to supercooled-state. *J. Phys.: Condens. Matter* **2008**, *20*, No. 335102.

- (52) Zhao, G.; Liu, C. S.; Zhu, Z. G. Local atomic structure and chemical bonding in liquid Te: An ab initio molecular-dynamics simulation. *Chem. Phys. Lett.* **2008**, *458*, 101–107.
- (53) Nørskov, J. K.; Bligaard, T.; Hvolbaek, B.; Abild-Pedersen, F.; Chorkendorff, I.; Christensen, C. H. The nature of the active site in heterogeneous metal catalysis. *Chem. Soc. Rev.* **2008**, *37*, 2163–2171.